Supplementary Materials for

Seismicity triggered by fluid injection–induced aseismic slip

Yves Guglielmi,* Frédéric Cappa,
Jean-Philippe Avouac, Pierre Henry, Derek Elsworth

*Corresponding author. E-mail: guglielmi@cerege.fr

This PDF file includes:

> Materials and Methods
> Figs. S1 to S6
> References

Other Supplementary Material for this manuscript includes the following:
(available at www.sciencemag.org/cgi/content/full/348/6240/1224/DC1)

> Database S1 as an Excel file

Materials and Methods

Measurements of fault movement and experiment setting

   Four boreholes, the injection hole and 3 seismic monitoring holes, respectively, were drilled vertically through the fault (Fig. 1a). A 1.5m long interval of the borehole crossing the fault was sealed by a straddle packer system. Fault slip and normal displacements were monitored with the SIMFIP probe (*13*) allowing simultaneous high-frequency (~500 Hz) sampling of 3D deformation across the fault, fluid pressures, and injection flow rates with sensitivities of 10^{-6} m in shear and dilatation, 10^3 Pa in pressure, and 0.1 l/min in flow rate. Three-dimensional movement of the fault is captured by a borehole-parallel extensometer set in the injection interval (Fig. 1b). The measurement system is anchored to the borehole wall by rings secured by compression keys. These rings are connected by variable-angled linkage-tubes that measure axial strains and enable triangulation of the full 3D displacement tensor. Linkage-tube deformations are captured with 15 fiber optic Bragg gratings that are attached to each tube and distributed along one single fiber that is also used to bring the Bragg sensor signals to the surface acquisition system. An inversion algorithm is used to calculate the relative three-dimensional displacements of the ring units from the tube deformations that are continuously monitored during the test. Then, the 3D-components of the displacement allow calculating the fault slip and dilation (Fig. 2). This was used to monitor fault slip during the experiment and to estimate the local state of stress from similar tests in adjacent boreholes. Indeed, following the Hydraulic Testing of Pre-existing Fractures method (HTPF, *17*), tests in adjacent holes yield an evaluation of the normal stress supported by fracture planes with different known orientations, and the complete stress evaluation results from an inversion of these results. Using the SIMFIP tool, we can accurately determine the onset of failure on the planes and both the normal and shear components of the induced movements. This approach yields that $\sigma_1 = 6 \pm 0.4$MPa is sub-vertical dips $80°S \pm 5°$, $\sigma_2 = 5 \pm 0.2$ MPa is sub-horizontal and strikes $N20°E \pm 10°$, and $\sigma_3 = 3 \pm 0.1$ MPa is sub-horizontal and strikes $N110°E \pm 10°$. Seismic signals are recorded at 8 kHz by a single 3-component accelerometer (S2: KB12VB, 0.15-260 Hz) and two 3-component geophones (S1: GS11D, 4.5-100Hz and S3: GS20DH, 40-1000 Hz). These sensors are set in the monitoring holes at 3 to 5 meters from the injection zone (Fig.1a). These three sensors

allow for a precise discrimination of seismic events in the near field of the injection source. Figure S1 shows two examples of captured micro-earthquakes (Fig. S1a) and long duration tremor-like seismic events (Fig. S1b).

Permeability estimation from modeling the injection

To study the fluid pressure and permeability changes in the fault, we developed a three-dimensional hydromechanical model of fluid pressure diffusion from the injection well. The finite-difference code FLAC^{3D} (*29*) is used to simulate fluid flow within discrete fractures/faults embedded in porous media and the resulting deformation. The code solves the fluid flow equation in three dimensions for a constant density (ρ_f = 1000 kg/m^3 for water) and dynamic viscosity (μ_f = 10^{-3}Pa.s for water) in heterogeneous and anisotropic media:

$$\nabla \cdot \left[\frac{\kappa_{ij}}{\mu_f} (\nabla p + \rho_f g \nabla x_i) \right] = S \frac{\partial p}{\partial t} - Q(t)$$

Where k_{ij} is the permeability, p is the fluid pressure, g is the acceleration of gravity, x_j reflects the position of a material point, t is the time, $Q(t)$ is the volumetric flow rate at the source, and S is the specific storativity that can be defined in its simplest form (S = γ ($\beta_s + \phi\beta_f$)) as a function of the pore compressibility (β_s), the fluid compressibility (β_f), and the specific weight of fluid (γ).

The model is 40 m ×40 m ×40 m on-edge with a fault plane having a dip angle of 70°. A horizontal-to-vertical stress ratio of 0.5 (i.e. extensional stress regime measured in the field, *13*) is set with the principal stress σ$_1$ vertical and parallel to the Z-axis of the model (Fig. S2a). The hydraulic boundaries are approximated as no-flow because the media is initially dry and the injection is local with a radius of hydraulic influence of some meters (*13*). The injection zone is represented as a vertical cylinder 1.5 m high and the measured in-situ flow rate-versus-time history is imposed at this point in the fault. The calculated pore pressure fields for each stabilized pressure step (yellow circles on Fig. S2b) are used for estimating the fault permeability (blue circles on Fig. 3a). We considered the fault main slip plane (Fig.1C) to be a 0.2m thick layer dipping 70°, and intersected by the injection interval. In this layer, the permeability tensor was considered isotropic with

3

initial permeability (before injection) being a factor of 25 higher than in the surrounding intact rock. Although isotropic, the flow is essentially one-dimensional along the fault, as conditioned by the low permeability of the encapsulating wall-rock. The bulk modulus of the fault is defined as the isotropic bulk modulus of this layer. This modulus was estimated by running a fully coupled hydromechanical model, and matching the calculated deformations to the ones measured at the low pressure steps with the HPPP probe before 1.6MPa when fault hydromechanical response is considered to be elastic. Figure S2c presents the evolution of the radius of pressurized fault zone, defined as the zone where the pore pressure exceeds 0.5MPa. Model results show that fault permeability increases by a factor of 20 over the duration of injection. This permeability evolution follows the growth of the slipping area (Fig. S3a).

Determination of fault friction

Based on our experimental measurements (fluid pressure and mechanical displacements), we can compute the shear ($\Delta\tau$) and normal stress ($\Delta\sigma_n$) changes for a circular crack of length (L) in an elastic medium with a shear (G) and a bulk (K) modulus as a function of the slip (δU_s) and opening (δU_n):

$$\Delta\tau = \frac{G\delta U_s}{L}$$

$$\Delta\sigma_n = \frac{K\delta U_n}{L}$$

The shear stress and normal stresses can then be calculated based on the initial stresses and assuming complete stress drop (Figure S3).

The moment (M_o) (Fig. 3b) can then be estimated from the fault slip and the slipping area ($A = \pi[L/2]^2$) (*30*):

$$M_o = G\delta U_s A$$

4

Figure S4a shows that the estimated friction is observed to increase with the sliding velocity suggesting a rate-strengthening behavior. Figure S4b shows no systematic trend with slip. We therefore exclude that slip has a first-order control on friction law and consider that the sliding velocity is the first-order controlling variable of friction.

The approximately linear trend is consistent with a logarithmic dependency of friction on sliding velocity as is most often observed in laboratory measurements of rock friction (e.g., *24*). The scatter must reflect noise measurements and possibly the influence of a state-dependency. We therefore tested a purely rate-strengthening friction law as well as rate-and-state friction laws.

With this 1D model, we find that fault slip is well reproduced with a purely rate-and-state friction law in the steady state regime, and that the introduction of the state variable does not improve significantly the fit to the data (Fig. 3d and S5).

We compare the fault slip and friction coefficient computed from the complete set of equations for the rate-and-state friction law with the aging and slip laws for evolution of the state variable (*31 - 32*), as well as a purely rate-strengthening friction law, equivalent to the steady-state frictional regime. The friction coefficient (μ) at slip rate (v) can be written:

$$\mu = \mu_o + a \ln \frac{v}{v_o} + b \ln \frac{v_o \theta}{d_c}$$

Where μ_o is the steady-state friction coefficient at reference slip rate (v_o), a and b are empirical dimensionless constants, d_c is the critical slip distance, and θ is a state variable which can be expressed by the "aging" or the "slip" law (*31*):

"Aging" law:

$$\frac{d\theta}{dt} = 1 - \frac{v\theta}{D_c}$$

"Slip" law:

$$\frac{d\theta}{dt} = -\frac{v\theta}{D_c} ln \frac{v\theta}{D_c}$$

In the steady-state regime, the friction coefficient is purely rate dependent, yielding:

$$\mu = \mu_o + (a - b)ln\frac{v}{v_o}$$

From these two friction laws, the corresponding slip (s) evolution over time (t) is, respectively:

$$s(t) = v_o \int_0^t e^{\left(\frac{\Delta\tau}{\sigma_n}+bln\left(\frac{\theta v_o}{d_c}\right)\right)/a} \cdot \Delta t$$

$$s(t) = v_o \int_0^t e^{\left(\frac{\Delta\tau}{(a-b)\sigma_n}\right)} \cdot \Delta t$$

We used a grid search method to invert the parameters (a and μ_0; v_0 fixed to the reference value of 10^{-7}m/s). The misfit between the observed (obs_i) and predicted ($pred_i$) fault slip is estimated with the reduced chi-square (χ^2), defined as:

$$\chi^2 = \frac{1}{N} \sum_{i=1,N} \left(\frac{obs_i - pred_i}{\sigma_i}\right)^2$$

With N is the number of experimental data (78) minus the number of rate-state parameters (2 for the steady-state regime (a and μ_o) and 4 (a, b, d_c and μ_o) for the full regime including the state variable), and σ_i is the uncertainties (10% for measurement and model). We set up the searching range from 0 to 0.07 for parameters a and b, from 0.1 to 0.9 for the reference friction coefficient (μ_o), and from 10^{-6} to 10^{-2} m for the critical slip distance (d_c). For the steady-state regime, we explored 3000 values for each parameters (a and μ_o), that is 9 million of solutions. For the state variable formalism, we explored 60

values for each parameters (a, b, μ_o, and d_c), that is about 13 million of solutions. The reduced chi-square of the fault slip, as a function of rate-state parameters (Fig. S5 and S6), has a well-defined global minimum at $a = 0.0447$ (+/-0.005) and $\mu_o = 0.67$ (+/-0.05) (for a reference velocity $v_0 = 10^{-7}$ m/s). Uncertainties correspond to a 68% confidence level and were estimated based on the Chi-squares statistics, corresponding to the parameters yielding a reduced chi-squares with 2.7/76 of the minimum value (red ellipse in Figure S6). These uncertainties ignore the uncertainty on the initial state of stress. Note that the minimum reduced Chi-squares is around 0.1, significantly less than unity, suggesting that the uncertainties on the measurement are probably overestimated by a factor of 3 or so. We didn't renormalize uncertainties so that our estimated uncertainties on the model parameters are probably overestimated as well.
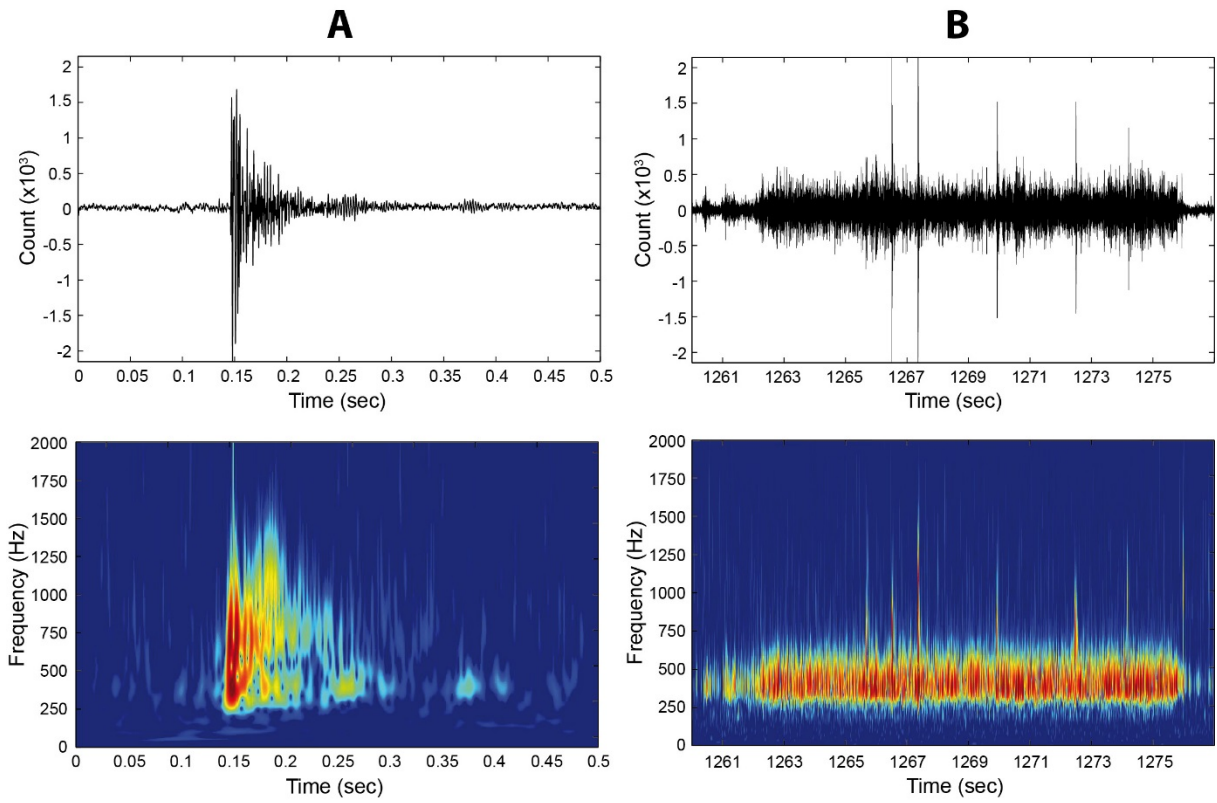
Fig. S1. Examples of signals and spectrograms: (**A**) micro-earthquakes and (**B**) tremor-like seismic events captured during the experiment.
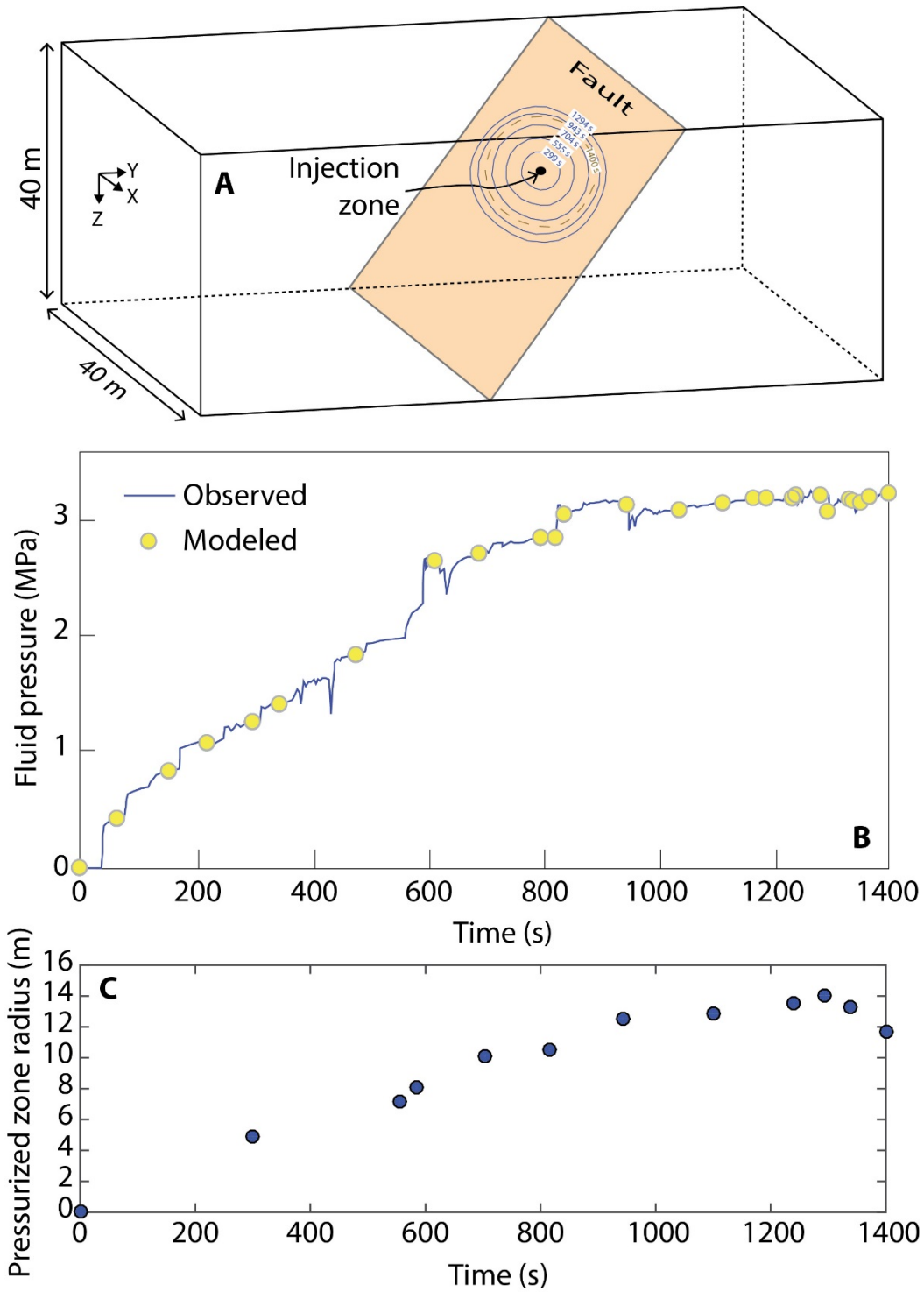
Fig. S2 Fluid injection model: (**A**) Set-up of the fluid injection model; (**B**) Measured (blue line) and modeled (yellow circle) fluid pressure to invert for permeability; (**C**) Evolution of the radius of pressurized fault zone, defined as the zone where the pore pressure exceeds 0.5MPa.
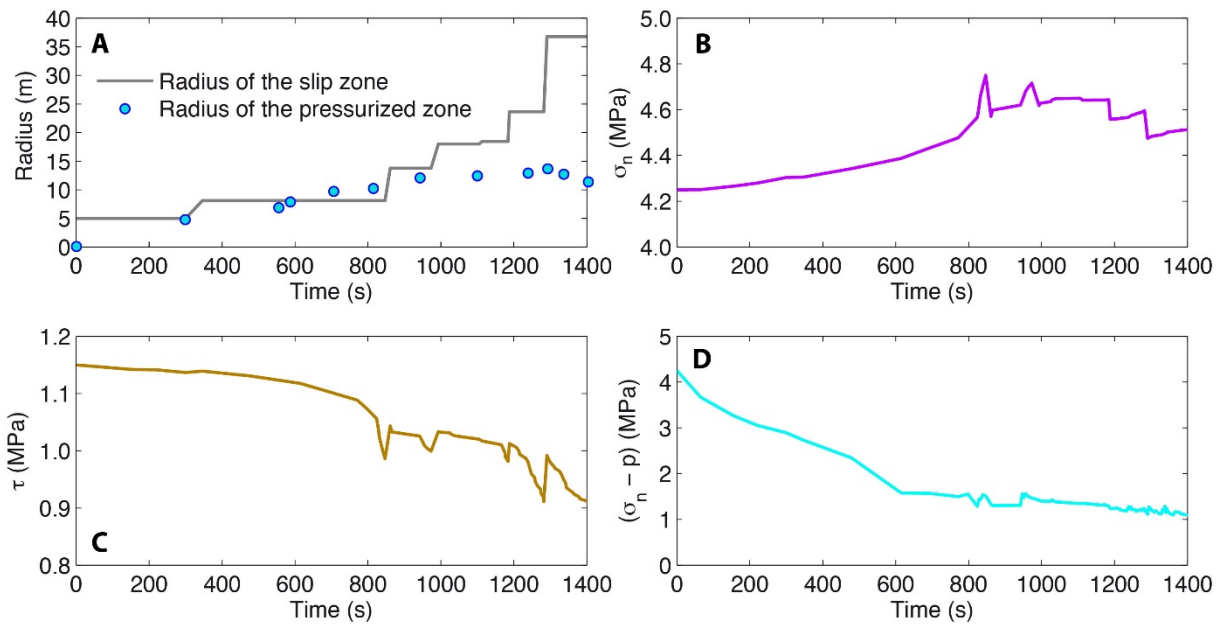
Fig. S3 Calculated fault flow geometry and stress variations: (**A**) Comparison of the estimated radius of the sliding zone and of the pressurized zone; (**B**) total normal stress; (**C**) shear stress; (**D**) effective normal stress.
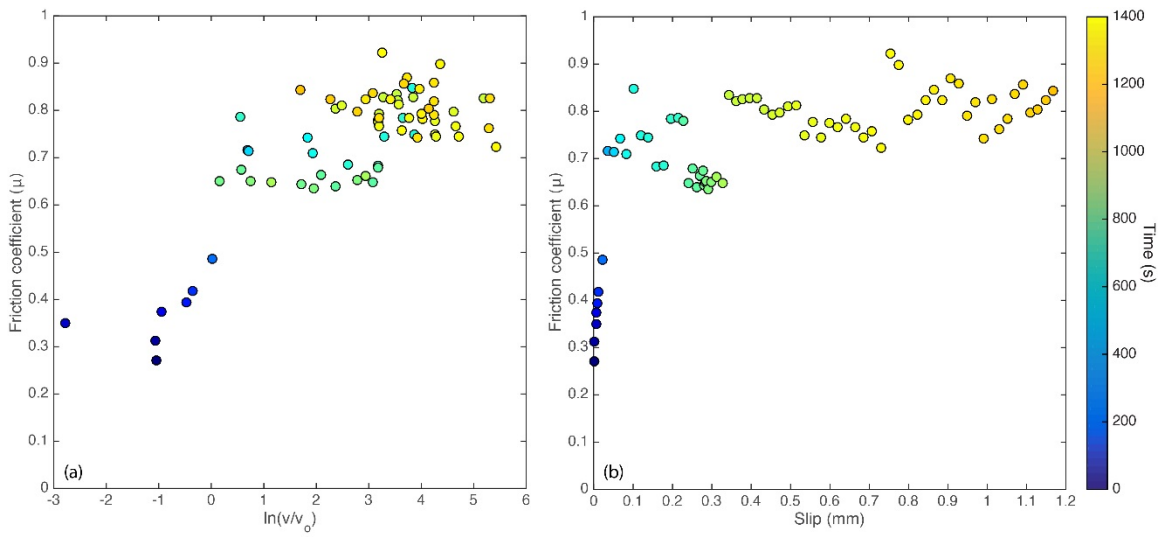
Fig. S4 Friction coefficient as a function of (a) sliding velocity and (b) slip.
Qualitatively the evolution of Fig.4a displays a better correlation than Fig.4b suggesting
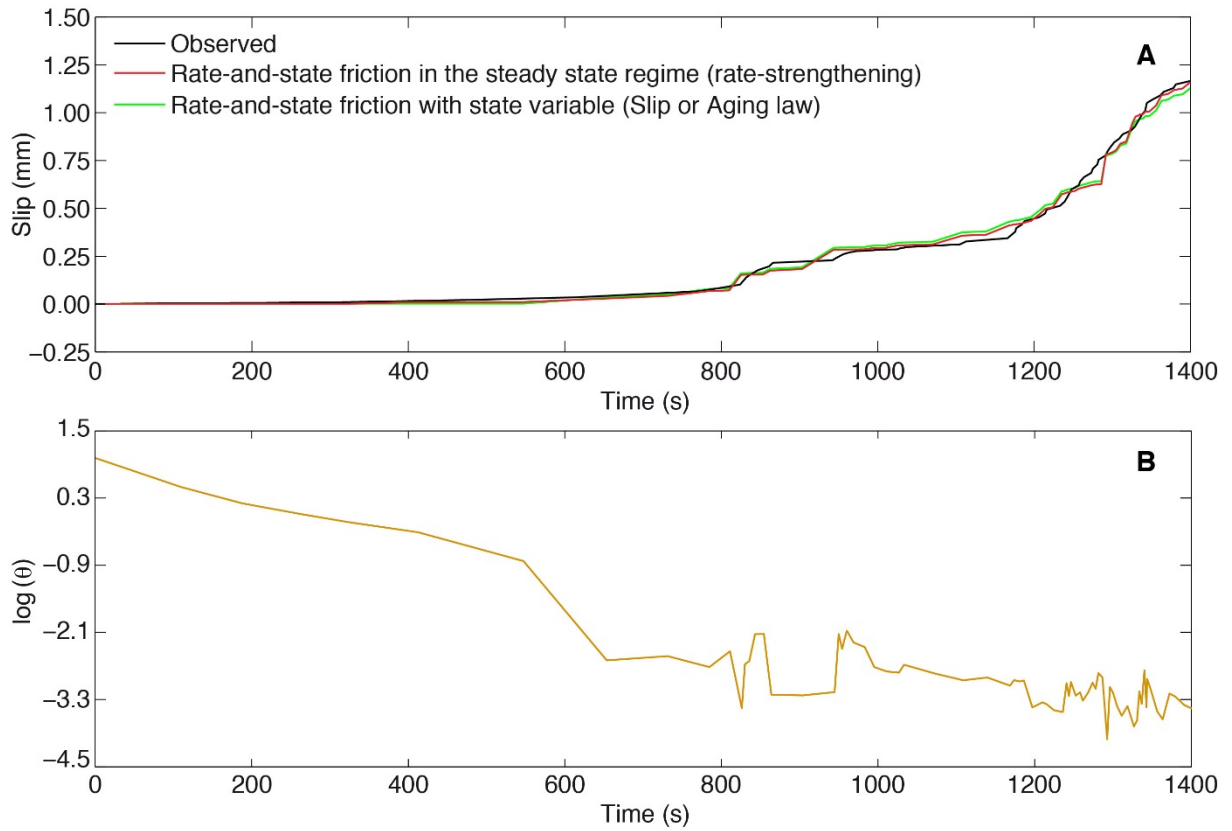that friction is governed more by slip-rate than slip during the experiment.

Fig. S5 Observed and modeled fault slip: (**A**) Observed and modeled fault slip assuming a purely rate-strengthening friction law or rate-and-state friction law (slip or aging law); (**B**) Evolution of the state variable *(θ)* with the rate-and-state friction law model.
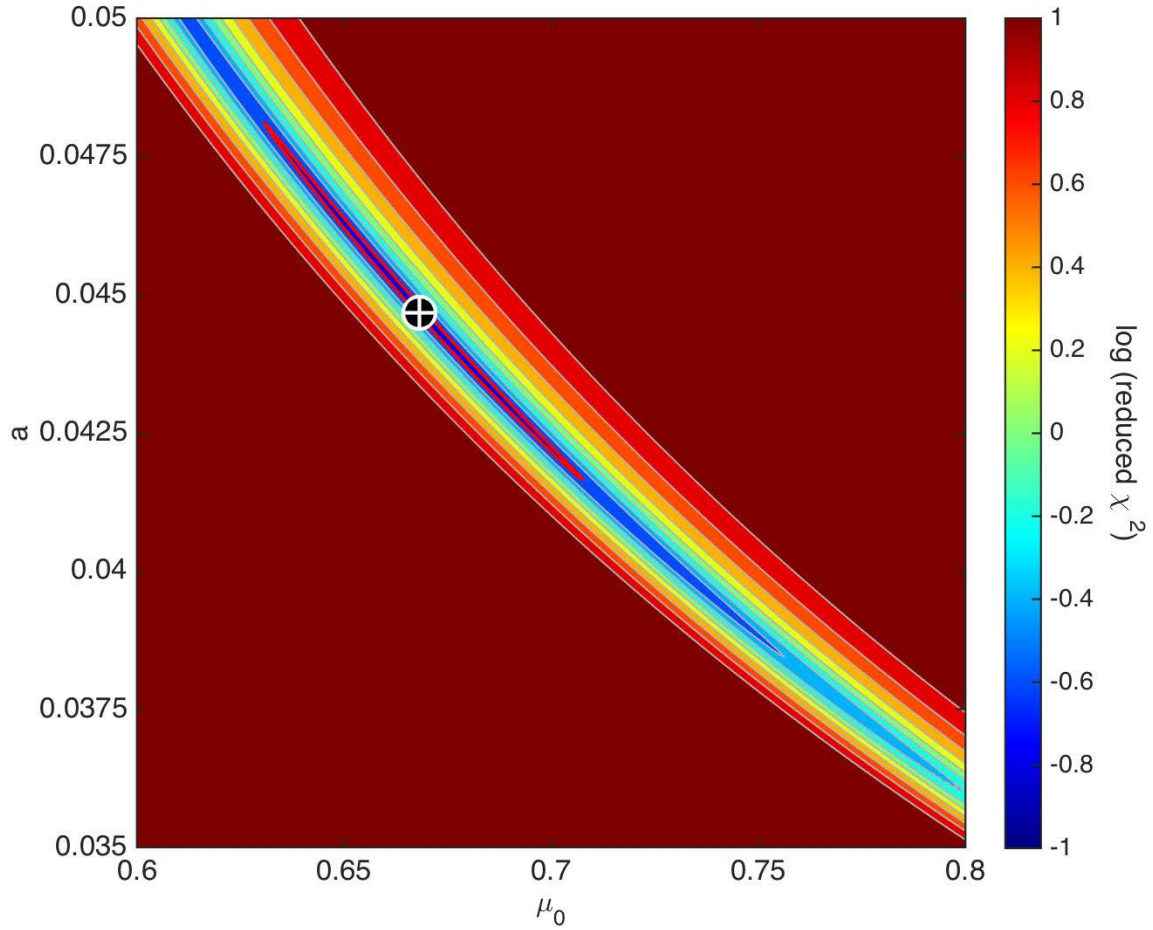
Fig. S6 Decimal log of the reduced chi-square (χ2) as a function of the model parameters for a purely rate-dependent friction law. The black dot with the white cross at $a = 0.0447$; $\mu_o = 0.67$ for a reference velocity $v_o = 10^{-7}$m/s. The red contour line corresponds to a confidence interval of 68%.

Database S1. Data table including time, flowrate, pressure, shear displacement, normal displacement, and number of seismic events.

References

1. C. B. Raleigh, J. H. Healy, J. D. Bredehoeft, An experiment in earthquake control at Rangely, Colorado. *Science* **191**, 1230–1237 (1976). Medline doi:10.1126/science.191.4233.1230

2. W. L. Ellsworth, Injection-induced earthquakes. *Science* **341**, 1225942 (2013). Medline doi:10.1126/science.1225942

3. C. Nicholson, R. L. Wesson, Triggered earthquakes and deep well activities. *Pure Appl. Geophys.* **139**, 561–578 (1992). doi:10.1007/BF00879951

4. F. H. Cornet, H. Helm, H. Poitrenaud, A. Etchecopar, Seismic and aseismic slips induced by large-scale fluid injections. *Pure Appl. Geophys.* **150**, 563–583 (1997). doi:10.1007/s000240050093

5. C. Nicholson, R. L. Wesson, Earthquake hazard associated with deep well injection: A report to the U.S. Environmental Protection Agency. *U.S. Geol. Surv. Bull.* 1951 (1990); http://pubs.usgs.gov/bul/1951/report.pdf.

6. E. Majer, R. Baria, M. Stark, S. Oates, J. Bommer, B. Smith, H. Asanuma, Induced seismicity associated with Enhanced Geothermal Systems. *Geothermics* **36**, 185–222 (2007). doi:10.1016/j.geothermics.2007.03.003

7. M. K. Hubbert, W. W. Rubey, Role of fluid pressure in mechanics of overthrust faulting. I. Mechanics of fluid-filled porous solids and its application to overthrust faulting. *Geol. Soc. Am. Bull.* **79**, 115–166 (1959).

8. H. Noda, N. Lapusta, Stable creeping fault segments can become destructive as a result of dynamic weakening. *Nature* **493**, 518–521 (2013). Medline doi:10.1038/nature11703

9. P. Segall, J. Rice, Dilatancy, compaction, and slip instability of a fluid-saturated fault. *J. Geophys. Res.* **100** (B11), 22155–22171 (1995). doi:10.1029/95JB02403

10. C. Scholz, Earthquakes and friction laws. *Nature* **391**, 37–42 (1998). doi:10.1038/34097

11. S. Bourouis, P. Bernard, Evidence for coupled seismic and aseismic fault slip during water injection in the geothermal site of Soultz (France), and implications for seismogenic transients. *Geophys. J. Int.* **169**, 723–732 (2007). doi:10.1111/j.1365-246X.2006.03325.x

12. M. Zoback, A. Kohli, I. Das, M. McClure, The importance of slow slip on faults during hydraulic fracturing stimulation of shale gas reservoirs, SPE 155476, Society of Petroleum Engineers, Americas Unconventional Resources Conference, Pittsburgh, PA, USA, 5–7 June 2012.

13. Y. Guglielmi, F. Cappa, H. Lancon, J. B. Janowczyk, J. Rutqvist, C. F. Tsang, J. Wang, ISRM suggested method for step-rate injection method for fracture in-situ properties (SIMFIP): Using a 3-components borehole deformation sensor. *Rock Mech. Rock Eng.* **47**, 303–311 (2014). doi:10.1007/s00603-013-0517-1

14. Laboratoire Souterrain à Bas Bruit, http://www.lsbb.eu

15. P. Jeanne, Y. Guglielmi, J. Lamarche, F. Cappa, L. Marie, Architectural characteristics and petrophysical properties evolution of a strike-slip fault zone in a fractured porous carbonate reservoir. *J. Struct. Geol.* **44**, 93–109 (2012). doi:10.1016/j.jsg.2012.08.016

16. Materials and methods are available as supplementary materials on *Science* Online.

17. B. C. Haimson, F. H. Cornet, ISRM suggested methods for rock stress estimation – Part 3: Hydraulic fracturing (HF) and/or hydraulic testing of pre-existing fractures (HTPF). *Int. J. Rock Mech. Min. Sci.* **40**, 1011–1020 (2003). doi:10.1016/j.ijrmms.2003.08.002

18. I. Das, M. Zoback, Long-period, long-duration seismic events during hydraulic fracture stimulation of a shale gas reservoir. *Leading Edge (Tulsa Okla.)* **30**, 778–786 (2011). doi:10.1190/1.3609093

19. J. Rutqvist, O. Stephansson, The role of hydromechanical coupling in fractured rock engineering. *Hydrol. J.* **11**, 7–40 (2003).

20. F. Cappa, Y. Guglielmi, J. Virieux, Stress and fluid transfer in a fault zone due to overpressures in the seismogenic crust. *Geophys. Res. Lett.* **34**, L05301 (2007). doi:10.1029/2006GL028980

21. F. Cappa, J. Rutqvist, Modeling of coupled deformation and permeability evolution during fault reactivation induced by deep underground injection of CO_2. *Int. J. Greenh. Gas Control* **5**, 336–346 (2011). doi:10.1016/j.ijggc.2010.08.005

22. O. Scotti, F. H. Cornet, In situ evidence for fluid-induced aseismic slip events along fault zones. *Int. J. Rock Mech. Min. Sci. Geomech. Abstr.* **31**, 347–358 (1994). doi:10.1016/0148-9062(94)90902-4

23. H. Perfettini, J. P. Avouac, Postseismic relaxation driven by brittle creep: A possible mechanism to reconcile geodetic measurements and the decay rate of aftershocks, application to the Chi-Chi earthquake, Taiwan. *J. Geophys. Res.* **109**, B02304 (2004). doi:10.1029/2003JB002488

24. C. Marone, Laboratory-derived friction laws and their application to seismic faulting. *Annu. Rev. Earth Planet. Sci.* **26**, 643–696 (1998). doi:10.1146/annurev.earth.26.1.643

25. C. Marone, C. Scholtz, R. Bilham, On the mechanics of earthquake afterslip. *J. Geophys. Res.* **96** (B5), 8441–8452 (1991). doi:10.1029/91JB00275

26. T. Tesei, C. Collettini, M. R. Barchi, B. M. Carpenter, G. Di Stefano, Heterogeneous strength and fault zone complexity of carbonate-bearing thrusts with possible implications for seismicity. *Earth Planet. Sci. Lett.* **408**, 307–318 (2014). doi:10.1016/j.epsl.2014.10.021

27. B. M. Carpenter, M. M. Scuderi, C. Collettini, C. Marone, Frictional heterogeneities on carbonate-bearing normal faults: Insights from the Monte Maggio Fault, Italy. *J. Geophys. Res. Solid Earth* **119**, 9062–9076 (2014). doi:10.1002/2014JB011337

28. B. A. Verberne, C. R. He, C. J. Spiers, Frictional properties of sedimentary rocks and natural fault gouge from the Longmen Shan Fault Zone, Sichuan, China. *Bull. Seismol. Soc. Am.* **100** (5B), 2767–2790 (2010). doi:10.1785/0120090287

29. Itasca Consulting Group, (2006), FLAC^{3D}, Fast Lagrangian Analysis of Continua in 3 Dimensions. Version 3.0. Five volumes. Minneapolis, Minnesota: Itasca Consulting Group.

30. J. D. Eshelby, The determination of the elastic field of an ellipsoidal inclusion and related problems. *Proc. R. Soc. London* **241**, 376–396 (1957). doi:10.1098/rspa.1957.0133

31. J. H. Dieterich, Modeling of rock friction, 1. Experimental results and constitutive equations. *J. Geophys. Res.* **84** (B5), 2161–2168 (1979). doi:10.1029/JB084iB05p02161

32. A. L. Ruina, Slip instability and state variable friction laws. *J. Geophys. Res.* **88** (B12), 10359–10370 (1983). doi:10.1029/JB088iB12p10359